applied sciences

MDPI

Article

High-Entropy Spinel Oxides Produced via Sol-Gel and Electrospinning and Their Evaluation as Anodes in Li-Ion Batteries

Beatrix Petrovičovà [1,†], Wenlei Xu [2,†], Maria Grazia Musolino [1], Fabiola Pantò [3], Salvatore Patanè [4], Nicola Pinna [2], Saveria Santangelo [1,5,*] and Claudia Triolo [1,5]

1 Dipartimento di Ingegneria Civile, dell'Energia, dell'Ambiente e dei Materiali (DICEAM), Università "Mediterranea", Loc., Feo di Vito, 89122 Reggio Calabria, Italy; beatrix.petrovicova@unirc.it (B.P.); mariagrazia.musolino@unirc.it (M.G.M.); claudia.triolo@unirc.it (C.T.)
2 Institut für Chemie and IRIS Adlershof, Humboldt-Universität zu Berlin, Brook-Taylor Straße 2, 12489 Berlin, Germany; xuwenlei@hu-berlin.de (W.X.); nicola.pinna@hu-berlin.de (N.P.)
3 Istituto di Tecnologie Avanzate per l'Energia (ITAE) del Consiglio Nazionale delle Ricerche (CNR), 98126 Messina, Italy; fabiola.panto@itae.cnr.it
4 Dipartimento di Scienze Matematiche e Informatiche, Scienze Fisiche e Scienze della Terra (MIFT), Università di Messina, 98166 Messina, Italy; salvatore.patane@unime.it
5 National Reference Center for Electrochemical Energy Storage (GISEL), Consorzio Interuniversitario Nazionale per la Scienza e Tecnologia dei Materiali (INSTM), 50121 Firenze, Italy
* Correspondence: saveria.santangelo@unirc.it
† These authors contributed equally to this work.

Abstract: In the last few years, high-entropy oxides (HEOs), a new class of single-phase solid solution materials, have attracted growing interest in both academic research and industry for their great potential in a broad range of applications. This work investigates the possibility of producing pure single-phase HEOs with spinel structure (HESOs) under milder conditions (shorter heat treatments at lower temperatures) than standard solid-state techniques, thus reducing the environmental impact. For this purpose, a large set of HESOs was prepared via sol-gel and electrospinning (by using two different polymers). Ten different equimolar combinations of five metals were considered, and the influence of the synthesis method and conditions on the microstructure, morphology and crystalline phase purity of the produced HESOs was investigated by a combination of characterization techniques. On the other hand, the presence of specific metals, such as copper, lead to the formation of minority secondary phase(s). Finally, two representative pure single-phase HESOs were preliminarily evaluated as active anode materials in lithium-ion batteries and possible strategies to enhance their rate capability and cyclability were proposed and successfully implemented. The approaches introduced here can be extensively applied for the optimization of HEO properties targeting different applications.

Keywords: high-entropy oxides; spinel oxides; electrospinning; sol-gel method; composite carbon/HEO nanofibers; lithium-ion batteries

Citation: Petrovičovà, B.; Xu, W.; Musolino, M.G.; Pantò, F.; Patanè, S.; Pinna, N.; Santangelo, S.; Triolo, C. High-Entropy Spinel Oxides Produced via Sol-Gel and Electrospinning and Their Evaluation as Anodes in Li-Ion Batteries. *Appl. Sci.* **2022**, *12*, 5965. https://doi.org/10.3390/app12125965

Academic Editor: Sergio Torres-Giner

Received: 11 May 2022
Accepted: 9 June 2022
Published: 11 June 2022

1. Introduction

The development of advanced materials with tailorable properties is a cornerstone of materials science and new technologies. Very recently, high-entropy materials (HEMs), a new class of materials obtained by using a configurational entropy-based design approach inherited from that of high-entropy alloys, have undergone an explosion of interest thanks to their unique structure and their novel and often unexpected functional properties [1–4]. HEMs are single-phase solid solutions stabilized in a multi-component system (generally, five or more elements in equimolar or near-equimolar ratio) by high configurational entropy. Numerous high-entropy compounds have been successfully synthesized and reported,

including nitrides [5,6], carbides [7,8] diborides [9], sulfides [10] and oxides [3,11–14]. In particular, starting with pioneering work by Rost et al. [11] published in 2015, high-entropy oxides (HEOs) have attracted growing interest in both academic research and industry for their potential to obtain intriguing multifunctional properties (such as thermal, electrochemical, dielectric, magnetic, catalytic and mechanical) resulting from high-entropy, lattice distortion, sluggish diffusion and cocktail effects, by exploiting a great number of possible element combinations [12,15–17]. The pioneering system was a single phase $(Mg_{0.2}Co_{0.2}Ni_{0.2}Cu_{0.2}Zn_{0.2})O$ solid solution with the rock-salt structure (*Fm-3m* symmetry), synthesized from five binary oxides (MgO, CoO, NiO, CuO, and ZnO) in equimolar proportions via a solid-state reaction route in the 850–900 °C temperature range [11]. Lower temperatures lead to a multiphase structure, rock-salt and tenorite (CuO), confirming that the increased configurational entropy was responsible for the thermodynamic stability of the rock-salt structure due the random distribution of cations on the specific sublattice sites.

So far, various HEOs with different crystal structures, such as spinel type [13,14,18], fluorite type [19,20], layered O_3-type [21], pyrochlore type [22] and perovskite type [23–25] structures have been synthesized using different synthetic routes. As previously mentioned, compared to conventional binary or doped transition metal oxide systems, HEOs exhibit amazing functional properties that can be finely tuned by varying their composition, such as "colossal dielectric constant" [26], very narrow band gap [27], high room temperature Li-ion conductivity [28], high temperature stability [29] and superior catalytic performance [30], making them potentially suitable for a wide range of applications, including energy storage, large-k dielectric materials, water splitting, catalysts, thermal protection and insulation [2,3].

For example, works from Sarkar [31] and Qiu [16] reported a higher reversible capacity and excellent cycling performance of the first rock-salt structured $(Mg_{0.2}Co_{0.2}Ni_{0.2}Cu_{0.2}Zn_{0.2})O$ HEO with respect to individual metal oxides, when it was used as anode materials in lithium-ion batteries (LIBs). The good electrochemical performance is ascribed to high configuration entropy that preserves the stability of the original crystal structure of the HEO during the charge/discharge processes. $(Ni_{0.2}Co_{0.2}Mn_{0.2}Fe_{0.2}Ti_{0.2})_3O_4$ with a spinel-structure, synthesized via solid-state sintering method by Chen et al. [32], as an anode material for LIBs, delivered a high capacity (~560 $mAhg^{-1}$) at a current density of 100 mAg^{-1} and exhibited an excellent capacity retention of 100% after 100 cycles, making it interesting for energy storage applications with high capacity and stability.

HEOs are most frequently prepared through the solid-state reaction. This method requires long heat treatments (typically 12–24 h [16,33–35]) at high temperatures (1000–1300 °C [16,33–35]) to crystallize the material, previously homogenized by grinding process(es) [34,35]) to obtain a random distribution of the cations in the HEO lattice and prevent the formation of secondary phase(s). These preparation conditions usually involve heavy sintering effects and particle agglomeration. Very recently, some authors have demonstrated that HEOs can be produced via simpler methods under milder conditions (shorter heat treatments at lower temperatures) than solid-state [36–39], thus reducing not only the effects of sintering on the size of the oxide particles, but also the environmental impact of the material production. Triolo et al. [36] have produced pure single-phase *rock-salt* $(Mg_{0.2}Co_{0.2}Ni_{0.2}Cu_{0.2}Zn_{0.2})O$ via the solvothermal method and electrospinning. Liu et al. [37] have synthesized single-phase *perovskite* $Ba(Ti_{0.2}Zr_{0.2}Sn_{0.2}Hf_{0.2}Ce_{0.2})O_3$ via the sol-gel method. Mesoporous *spinel* $(Ni_{0.2}Co_{0.2}Cr_{0.2}Fe_{0.2}Mn_{0.2})_3O_4$ nanospheres have also been obtained using the same method [40]. The preparation of single-phase *fluorite* $(La_{0.2}Nd_{0.2}Sm_{0.2}Dy_{0.2}Yb_{0.2})_2Zr_2O_7$ [38] and bixbyite $(Y_{0.2}Yb_{0.2}Sm_{0.2}Eu_{0.2}Er_{0.2})_2O_3$ [39] electrospun nanofibers has been also reported.

This work demonstrates that a large set of high-entropy oxides with *spinel* structure (HESOs) can be obtained using the sol-gel method and, for the first time, electrospinning. Being solution-based, both synthesis techniques allow for the easy preparation of homogeneous multi-component oxides. Besides, they are suitable for large-scale material manufacturing since they are scalable and consist of two sequential steps (namely, sol-gel

preparation/fibrous film deposition and heat treatment) that, in an industrial production chain, can progress simultaneously. In syntheses via electrospinning, a technique particularly suitable for the manufacturing of fibrous nanostructured materials with high aspect-ratio and surface-area [41], two polymers (polyvinylpyrrolidone and polyacrylonitrile) are used to investigate the influence of the polymer on the formation of fibers and on their microstructure. Ten different equimolar combinations are considered, each containing five metals selected from Mg, Ti, Cr, Mn, Fe, Co, Ni, Cu and Zn. Their choice is operated by selecting cations with a similar ionic radius and a good chemical compatibility. The produced HESOs are analyzed by complementary techniques to investigate how the synthesis method and conditions influence their structure, morphology and crystalline phase. Since the results of their preliminary evaluation as active anode materials in LIBs indicate that the materials need to be improved by optimizing their preparation conditions, herein, two strategies are proposed to enhance the rate capability and cyclability of two representative samples. The first strategy is to add lithium into the HESO lattice, as the multi-valence nature of the HESO constituent elements promotes the formation of oxygen vacancies, known to favor Li^+ transport [32]. The second (conventional) strategy is to embed the HESO particles in a carbonaceous matrix [42–44]. Both the strategies are successfully implemented.

2. Materials and Methods

2.1. Reagents and Chemicals

The following reagents were utilized as metal sources for the preparation of HESO-samples: magnesium (II) acetate tetrahydrate, $Mg(CH_3COO)_2{\cdot}4H_2O$ (purity: 98%; CAS No. 16674-78-5, Sigma Aldrich, Burlington, MA, USA); titanium (IV) butoxide, $Ti(C_4H_9O)_4$ (purity: 97%; CAS No. 5593-70-4); chromium (III) acetate hydroxide, $Cr_3(OH)_2(CH_3COO)_7$ (purity: 98%; CAS No. 39430-51-8, Sigma Aldrich); manganese (II) acetate tetrahydrate, $Mn(CH_3COO)_2{\cdot}4H_2O$ (purity: 99%; CAS No. 6156-78-1, Sigma Aldrich); iron (II) acetate, $Fe(CH_3COO)_2$ (purity 95%; CAS No. 3094-87-9 Sigma Aldrich); cobalt (II) acetate tetrahydrate, $Co(CH_3COO)_2{\cdot}4H_2O$ (purity: 99%; CAS No. 6147-53-1, Sigma Aldrich); nickel (II) acetate tetrahydrate, $Ni(CH_3COO)_2{\cdot}4H_2O$ (purity: 98%; CAS No. 6018-89-9, Sigma Aldrich); copper (II) acetate, $Cu(CH_3COO)_2$, (purity: 98%; CAS No. 142-71-2, Sigma Aldrich); zinc (II) acetate dihydrate, $(CH_3COO)_2Zn{\cdot}2H_2O$ (purity: 98%; CAS No. 5970-45-6, Fischer Scientific, Hampton, NH, USA). In addition, lithium acetate, $Li(CH_3COO)$ (purity: 99.95%; CAS No. 546-89-4, Sigma Aldrich) was used as a lithium source to prepare a lithiated HESO-sample.

Citric acid monohydrate, $HOC(COOH)(CH_2COOH)_2{\cdot}H_2O$ (purity: 98%; CAS No. 5949-29-1, Sigma Aldrich), was used as a complexing agent for the preparation of HESO-samples via the sol-gel method.

The solution for the synthesis of electrospun samples was prepared by utilizing polyacrylonitrile, $(C_3H_3N)n$ (average molecular weight: 150,000 g mol^{-1}; purity: 99.9%; CAS No. 25014-41-9, Sigma Aldrich), or polyvinylpyrrolidone, $(C_6H_9NO)_n$ (average molecular weight: 1,300,000 g mol^{-1}; purity: 98%; CAS No. 9003-39-8, Sigma Aldrich), as a polymer. In the former case, N,N-dimethylformamide, $HCON(CH_3)_2$ (anhydrous: 99.8%; CAS No. 68-12-2, Sigma Aldrich), acted as a solvent. In the latter, a mixture of N,N-dimethylformamide and ethanol, CH_3CH_2OH (purity: 99.5%; CAS No. 64-17-5, Sigma Aldrich), was used.

All chemicals were used without any further purification.

2.2. Syntheses of HESO-Samples

Table 1 reports the selected equimolar combinations of five metals and the codes of the HESO-samples produced. The suffix sg marks the HESOs prepared by the sol-gel method. In the case of the electrospun HEOs, the suffixes a and b identify the samples prepared by using polyvinylpyrrolidone (PVP) or polyacrylonitrile (PAN) as a polymer, respectively.

Table 1. Codes of samples prepared by sol-gel method (SG) method and electrospinning (ES) by using PVP or PAN as a polymer.

Selected Element Combination									Single/Main Oxide Phase	Sample Codes		
Mg	Ti	Cr	Mn	Fe	Co	Ni	Cu	Zn		SG	ES	
											PVP	PAN
■	■			■	■		■	■	$(Mg_{0.2}Ti_{0.2}Fe_{0.2}Cu_{0.2}Zn_{0.2})_3O_4$	5MA-sg	–	–
			■	■	■	■		■	$(Mn_{0.2}Fe_{0.2}Co_{0.2}Ni_{0.2}Zn_{0.2})_3O_4$	5MD-sg	5MD-a	5MD-b
		■	■	■	■	■			$(Cr_{0.2}Mn_{0.2}Fe_{0.2}Co_{0.2}Ni_{0.2})_3O_4$	5ME-sg	5ME-a	5ME-b
		■	■	■	■			■	$(Cr_{0.2}Mn_{0.2}Fe_{0.2}Co_{0.2}Zn_{0.2})_3O_4$	5MF-sg	5MF-a	5MF-b
		■	■	■		■		■	$(Cr_{0.2}Mn_{0.2}Fe_{0.2}Ni_{0.2}Zn_{0.2})_3O_4$	5MG-sg	–	5MG-b
	■		■	■			■	■	$(Ti_{0.2}Mn_{0.2}Fe_{0.2}Cu_{0.2}Zn_{0.2})_3O_4$	5MH-sg	–	–
■		■	■	■		■			$(Mg_{0.2}Cr_{0.2}Mn_{0.2}Fe_{0.2}Ni_{0.2})_3O_4$	5MI-sg	–	–
■			■	■	■				$(Mg_{0.2}Cr_{0.2}Mn_{0.2}Fe_{0.2}Co_{0.2})_3O_4$	5MJ-sg	–	–
	■		■	■	■	■			$(Ti_{0.2}Mn_{0.2}Fe_{0.2}Co_{0.2}Ni_{0.2})_3O_4$	5MK-sg	5MK-a	–
			■	■		■	■	■	$(Mn_{0.2}Fe_{0.2}Ni_{0.2}Cu_{0.2}Zn_{0.2})_3O_4$	5ML-sg	5ML-a	5ML-b

2.2.1. Syntheses by the Sol-Gel Method

In the syntheses of HESO samples via the sol-gel (SG) method, stoichiometric amounts of the selected five metals were dissolved in 30 g water, one at a time (Figure S1a). After magnetic stirring at 350 rpm for 1 h, 3.5 g citric acid was added and the resulting mixture was further stirred (350 rpm) at 90 °C until a gel was formed (about 1 h). The as-obtained gel was dried at 80 °C overnight and, subsequently, calcined in static air at 350 °C for 2 h, at 500 °C for 2 h, at 800 °C for 2 h and at 900 °C for 2 h (Figure S1(c1)), finally obtaining powders consisting of HESO particles (Figure S1(d1)), having spinel structure as a unique/primary phase (Figure S1e). Note that the treatment at the highest temperature (lower than in the conventional solid reaction [16,33–35]) lasts only 2 h, i.e., a much shorter time than that necessary to produce HESOs by the frequently utilized solid-state approach (typically 12–24 h [16,33–35,45,46]). The same consideration applies to the case of electrospun samples.

In the case of the lithiated sample (Li-HESO), $Li(CH_3COO)$ was dissolved in an aqueous solution containing the selected five metals salts. Then, the same preparation steps as for the unlithiated samples were carried out.

2.2.2. Syntheses by Electrospinning

In syntheses via electrospinning (ES), two different polymer/solvent solutions were evaluated, namely PAN/N,N-dimethylformamide (DMF) and PVP/DMF+ethanol (EtOH). In the latter case, the spinnable solution was obtained by dissolving PVP (25 wt%) in EtOH and the metal salts were separately dissolved in DMF. Both solutions were magnetically stirred at 350 rpm at room temperature (RT) until they became clear. Then, they were mixed under continuous stirring (350 rpm) for 2 h. The PAN/DMF solution was prepared by dissolving PAN (7.1 wt%) in DMF. Then, proper amounts of the metallic salts were added (Figure S1a), one at a time, under continuous stirring (350 rpm) until a homogeneous spinnable solution containing the selected equimolar combination of five metals was obtained (about 1 h). Regardless of the metal combination selected, the total amount of metals was kept constant (38.5 wt% relative to PAN and 24.7 wt% relative to PVP). After slow mixing overnight at RT, the solution was ready for deposition.

Each homogeneous spinnable solution obtained was loaded into a 20 mL syringe equipped with a 40 mm long 0.8 mm gauge stainless-steel needle. Electrospinning (Figure S1c2) was carried out, at 22 ± 1 °C and 40% relative air humidity, by using a CH-01 Electro-spinner 2.0 (Linari Engineering s.r.l.). The solution feeding rate, applied DC voltage and needle-collector distance were fixed at 23.5 μL min^{-1}, 15 kV and 11 cm, respectively. The pristine polymer/metal salts nanofibers (NFs) were ejected from the needle and collected over an aluminum foil to form a non-woven fibrous membrane.

After drying at RT overnight to remove the solvent residuals, the as-spun membrane was peeled from the collector and calcined in static air (Figure S1(c2)). A four-step heating process was operated in the case of PVP-derived HESO-samples (350 °C for 2 h, 500 °C for 2 h, 800 °C for 2 h and 900 °C); PAN-derived HESO-samples were obtained through a two-step heat-treatment (700 °C for 2 h and 900 °C for 2 h). The obtained powders consisted of porous architectures, generally built up by HESO-NFs (Figure S1(d2)) with spinel structure as a unique/primary phase (Figure S1e).

In addition to pure HEO-samples, a composite carbon/HESO sample was prepared. For this purpose, the same PAN/DMF-based solution as for the corresponding pure HESO was used, but after the as-spun membrane had been detached from the collector, it was first stabilized in air at 225 °C [42] for 2 h, and subsequently carbonized under inert atmosphere through the same two-step heat-treatment as for pure HESO samples, so that the oxide grains formed in the composite NFs experienced the same temperatures as in those of pure oxide.

2.3. Characterization

After thermal processing, the produced HESO-samples were analyzed by means of a number of complementary techniques. A Phenom Pro-X scanning electron microscope, equipped with an energy-dispersive X-ray (EDX) spectrometer, was used to investigate the texture and morphology of HESO-samples by means of scanning electron microscopy (SEM). High-resolution transmission electron microscopy (HRTEM), high-angle annular dark-field scanning transmission electron microscopy (HAADF-STEM), selected-area electron diffraction (SAED) and energy dispersive X-ray spectroscopy (EDX) elemental mappings were carried out on a FEI Talos F200S scanning/transmission electron microscope, operated at 200 kV.

The crystalline phases of the HESO-samples were identified by X-ray diffraction (XRD) and micro-Raman spectroscopy (MRS). A Bruker D2 Phaser diffractometer, equipped with a Ni β-filtered Cu-Kα radiation source, was used to record XRD patterns, whereas JCPDS database of reference compounds allowed for the diffraction-peak identification. A NT-MDT NTEGRA Spectra SPM spectrometer, equipped with MS3504i 350 mm monochromator and ANDOR Idus CCD, was used to measure Raman scattering excited by a solid-state laser operating at 532 nm. Raman measurements were carried out in reflection mode using a Mitutoyo high numerical aperture 100× objective to excite and collect the scattered signal from the sample surface. The acquired signal was dispersed by an optical grating (600 lines/mm) and, finally, detected by the cooled CCD. The use of a very low laser power (250 μW at the sample surface) prevented local heating of the samples and annealing effects.

2.4. Electrochemical Characterization

Electrochemical properties of HEOs were evaluated using CR2032-type coin cells, which were assembled in an Ar-filled glovebox. First, 70% active materials (HESO), 20% conductive carbon black (Super P, Timcal, Billerica, MA, USA) and 10% polyvinylidene fluoride (PVDF, Alfa Aesar, Karlsruhe, Germany) were homogeneously mixed with N-methyl-2-pyrrolidone (NMP, anhydrous 99.5%, Sigma-Aldrich, Steinheim, Germany). The resulting slurry was uniformly cast on Cu foil (Goodfellow, Hamburg, Germany) with a doctor blade apparatus and then dried in a vacuum oven at 60 °C for 1 h. After a cold-laminating step, electrodes with a diameter of 12 mm were punched out and dried overnight at 120 °C under vacuum using a Büchi glass oven. The mass loading of active material was ≈ 1.5 mg cm^{-2}. Lithium metal foil was used as both counter and reference electrodes. 1 M $LiPF_6$ (99.9% battery grade, ABCR, Karlsruhe, Germany) solution in a mixture of ethylene carbonate (EC, 99.9%, ABCR), diethyl carbonate (DEC, 99.9%, ABCR) and dimethyl carbonate (DMC, 99.9%, ABCR) with a 1:1:1 volume ratio was used as the electrolyte. A glass microfiber filter (Whatman, Steinheim, Germany) was used as a separator.

Galvanostatic charge–discharge (GCD) cycling was carried out at room temperature using a CT2001 A battery testing system (Landt Instruments, Wuhan, China). Cyclic voltammograms (CVs) were measured on a Bio-Logic (Seyssinet-Pariset, France) VMP3 multichannel potentiostat/galvanostat with a built-in electrochemical impedance spectroscopy (EIS) analyzer. EIS was tested at open-circuit potential (OCP), in the frequency range of 100 kHz to 0.1 Hz with an amplitude of 10 mV.

3. Results

3.1. Morphology

Figure 1 shows some representative SEM micrographs of the produced samples. The SG method favors the formation of porous sponge-like structures (Figure 1a–d), mainly consisting of agglomerates of small particles. In the case of ES (Figure 1e–k), the use of PVP and PAN leads to different selectivity towards the formation of NFs. Fibrous structures are always observed in PAN-derived samples (Figure 1j–l), where beads rarely form. On the contrary, in some of the PVP-derived samples, fibers are hardly observed (Figure 1e,g), whereas, in the remaining ones, NFs and beaded structures often coexist (Figure 1f,i); in some samples, fibers are organized in a three-dimensional network (Figure 1h,i).

Figure S2 shows the NF diameter distributions as automatically estimated by the analysis software of the SEM microscope. In PVP-derived samples, the distributions are centred on values increasing in the order 5MK-a (580 nm) < 5ME-a (630 nm) < 5ML-a (770 nm). In PAN-derived samples, the distribution centre values increase in the order 5MG-b (380 nm) < 5MF-b (510 nm) < 5MD-b (520 nm) < 5ME-b (660 nm) < 5ML-b (720 nm). The comparison of the results relative to samples 5ME-a and 5ML-a with those relative to samples 5ME-b and 5ML-b suggests a possible role of the metal combination in determining the variation of the NF diameter.

Regardless of the sample morphology, preparation method and conditions, the dispersion of the composing elements is always spatially uniform within the samples, as revealed by SEM/EDX analysis (Figure S3).

Figure 2 displays some representative HRTEM images of the investigated samples. Images with lower magnification are shown in Figure S4a–d. Regardless of their composition, samples produced by the SG route consist of aggregates of crystalline oxide particles (see the SAED pattern in the inset of Figure S4a), having polyhedral shape and size ranging between a few tens of nm to hundreds of nm (Figure 2a,e). The electrospun PAN-derived NFs are micrometers long and have diameters ranging between 150 and 450 nm. Independent of their composition, they are built-up by interconnected crystalline oxide grains (see the SAED patterns in the insets to Figure S4b–d) with similar shape and size to that of particles synthesized by the SG method (Figure 2b–d,f–h). For both synthesis routes, the STEM/EDX elemental maps (Figure S5) prove the homogeneity of the spatial distribution of metals and oxygen at the nanometer scale.

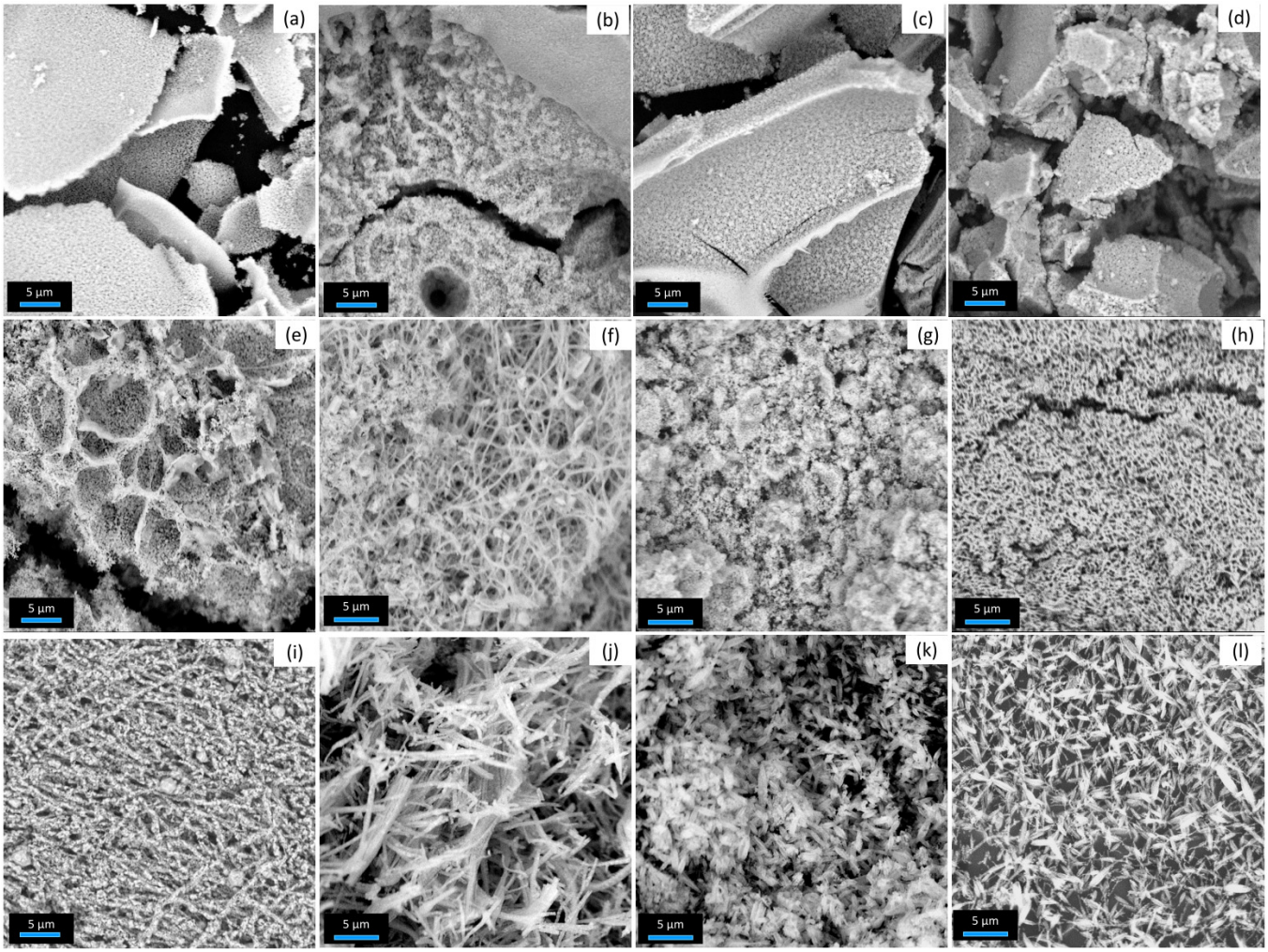

Figure 1. SEM micrographs of samples (**a**) 5MD-sg, (**b**) 5ME-sg, (**c**) 5MF-sg, (**d**) 5MK-sg, (**e**) 5MD-a, (**f**) 5ME-a, (**g**) 5MF-a, (**h**) 5MK-a, (**i**) 5ML-a, (**j**) 5ME-b, (**k**) 5MF-b and (**l**) 5MG-b.

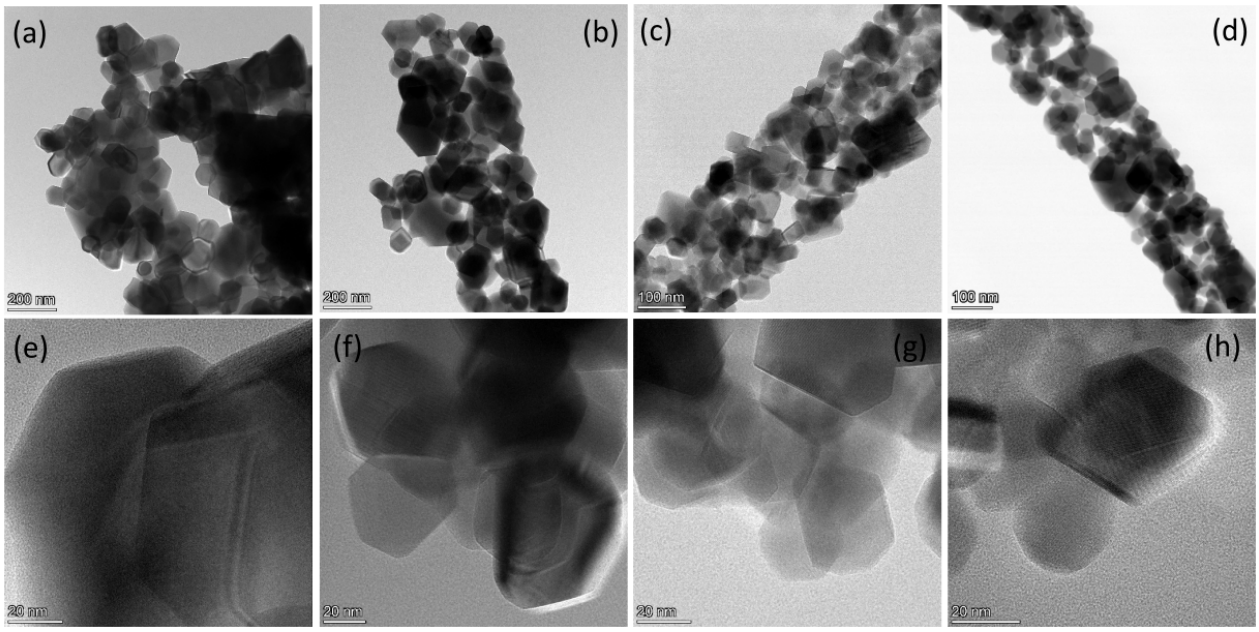

Figure 2. HRTEM images of samples (**a**,**e**) 5MF-sg, (**b**,**f**) 5ME-b, (**c**,**g**) 5MF-b and (**d**,**h**) 5MG-b.

3.2. Phase of the Oxide

Figure 3 shows the results of XRD analysis on all samples. In particular, the diffractograms of samples prepared via the SG method are displayed in Figure 3a, whereas Figure 3b,c report the XRD patterns of electrospun samples derived from PVP and PAN, respectively. Regardless of both methods and details of the preparation, reflections at ca. 18.3°, 30.2°, 35.6°, 37.2°, 43.3°, 53.7°, 57.3°, 63.0°, 71.5°, 74.6° and 75.6° 2θ-angles are detected in all patterns. They are the reflections from 111, 220, 331, 222, 400, 422, 511, 440, 620, 533 and 622 planes of the face-centered cubic (fcc) spinel structure, *Fd-3m* space group (JCPDS no. 22-1084) [45,47–52].

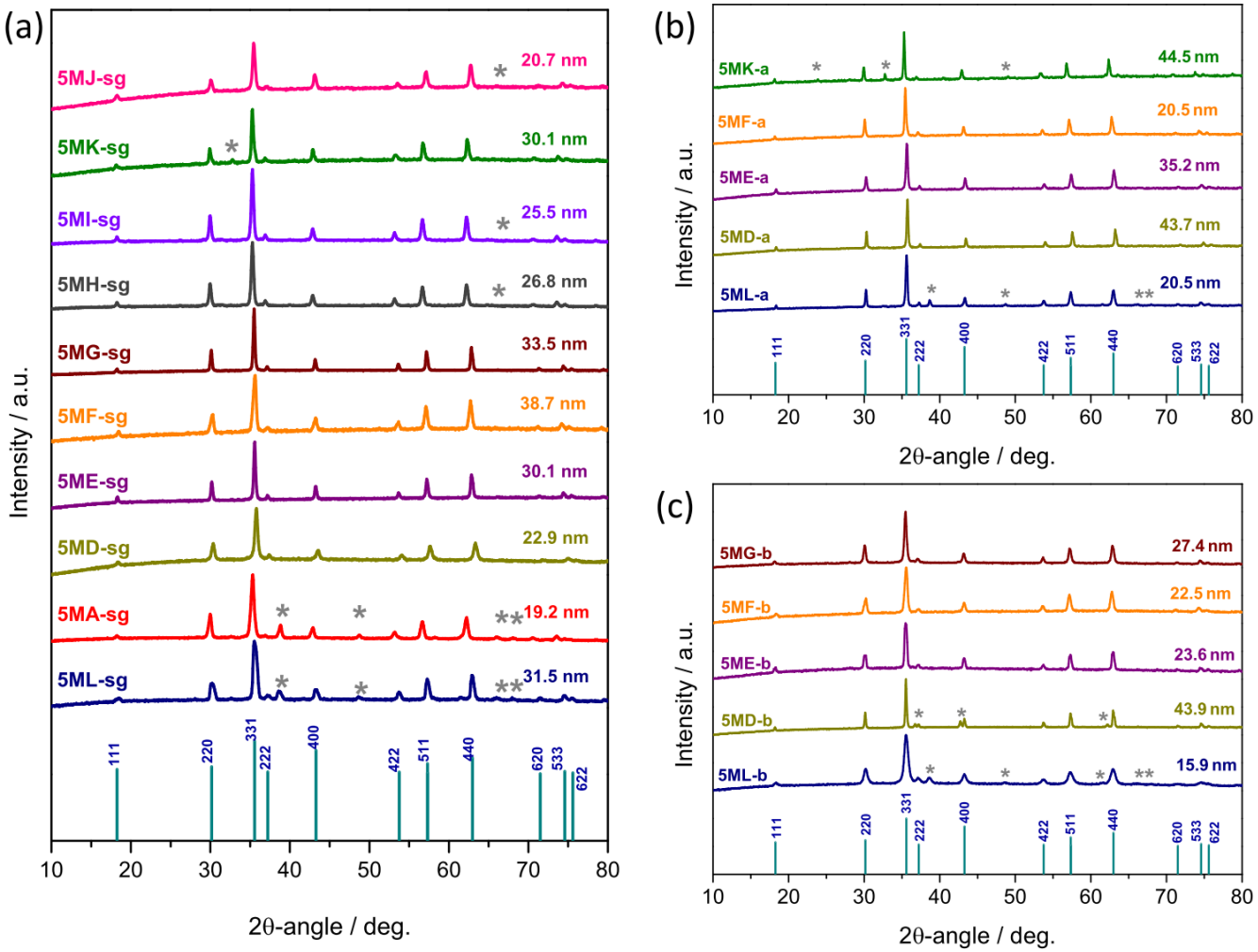

Figure 3. XRD patterns of the samples produced via (**a**) sol-gel method and (**b**,**c**) electrospinning by the use of (**b**) PVP and (**c**) PAN as a polymer. Stars mark reflections not assignable to the spinel phase.

In most samples, no additional reflections are detected, which proves that the spinel phase is the unique crystalline phase formed. On the contrary, in samples 5MA-sg, 5MK-sg, 5ML-sg (Figure 3a), 5MKa, 5ML-a (Figure 3b), 5ML-b and 5MD-b (Figure 3c), the detection of weaker additional reflections reveals the formation of secondary phases. Interestingly, this seems to be a common feature of the diffractograms of samples having the same nominal composition (e.g., 5ML-sg, 5ML-a and 5ML-b). The reflections, detected in the XRD patterns of 5ML-sg, 5ML-a and 5ML-b at 32.6°, 38.6°, 48.6°, 61.6°, 66.0° and 67.9° (owing to the scale, only the most intense of them are visible in Figure 3), are from

100, 101, 102, 200, 112 and 201 planes of the monoclinic structure of CuO (JCPDS No. 45-0937) [53,54]. The presence of Cu among the five selected metals promotes the formation

of CuO as a secondary phase also in sample 5MA-sg and 5MH-sg. In 5MI-sg and 5MJ-sg, a weak reflection from the 112 planes of α-Mg is detected at 66° [55,56].

In sample 5MK-sg, an additional reflection is visible at 32.8°; in sample 5MK-a, besides it, reflections at 23.8° and 49.1° are also detected. They are reflections from 211, 222 and 431 crystallographic planes of the body-centered cubic (bcc) structure of Mn_2O_3 (JCPDS No. 89-4836) [57,58].

The behavior of sample 5MD-b differs from that of the samples with the same nominal composition. Reflections 222, 400 and 440 seem to be split owing to the appearance of very close signals at ca. 36.8°, 42.7° and 62.2°. Their detection might be indicative either of the existence of two spinel sublattices or of the segregation of some metal(s) in a secondary phase. In the latter case, the reflections might originate from 111, 200 and 220 planes of nickel oxide (NiO, JCPDS No. 04-0835) [59,60] and/or cobalt oxide (CoO, JCPDS No. 78-0431) [61], both characterized by the same fcc crystalline structure.

Rietveld refinements from XRD data (Figure S6) were carried out to assess the relative amount of the secondary phase(s). The results obtained are reported in Table S1. In samples produced via the SG method, secondary phases reach 12.4%, while in electrospun samples their percentage is 7.3–8.8%.

For all samples, the mean sizes of the HESO crystallites are calculated from the most intense reflection through the Scherrer's equation [60]. The values obtained, reported in Figure 3, range from 19.2 to 38.7 nm for HESOs produced via the SG method. For electrospun samples, the mean sizes of the crystallites vary in the ranges 20.5–44.5 nm and 15.9–27.4 nm, for PVP- and PAN-derived HESOs, respectively.

For a given metal combination, the observed variations of crystallite sizes do not follow any general trend or dependence on the preparation method. As an example, in the 5MD-series, the mean crystallite size increases in the order 5MD-sg (22.9 nm) < 5MD-a (43.7 nm) < 5MD-b (43.9 nm), whereas in the 5MF-series, it varies in the order 5MF-sg (38.7 nm) > 5MF-b (22.5 nm) > 5MF-a (20.5 nm).

Additional information on the phase-purity of the prepared samples and its spatial homogeneity is inferred by measuring Raman scattering from several random locations in each specimen (Figure S7). No appreciable differences in the relative intensities and in the positions of the bands at the probed locations are observed in pure single-phase samples (Figure S7a,b). On the contrary, changes in the spectral profile at a random location indicate local deviations from the average chemical composition and segregation in a secondary phase (Figure S7c). The obtained results by these measurements are in agreement with the indications emerged from the XRD analysis.

Figure 4 shows the averaged Raman spectra of pure single-phase samples, obtained from the spectra acquired at random locations in each sample. These spectra provide a global picture of the entire sample. The vibration modes theoretically predicted for the spinel-group [62,63] include five Raman-active phonon modes, namely three triply degenerate modes having F_{2g} symmetry, one doubly degenerate mode with E_g-symmetry and an A_{1g}-symmetry mode. The lowest frequency $F_{2g}(1)$ mode might be due to the translation motion of the BO group [64] or originate from a complete translation of the AO_4 unit within the spinel lattice [65,66]. The E_g mode is associated with symmetric bending of O anion with respect to octahedral B cation [67,68]. Higher frequency $F_{2g}(2)$ and $F_{2g}(3)$ modes arise from the asymmetric stretching and asymmetric bending of oxygen, respectively [65,67,69]. Finally, the A_{1g} mode is attributed to the vibration along the direction joining an oxygen atom to the tetrahedral A cation.

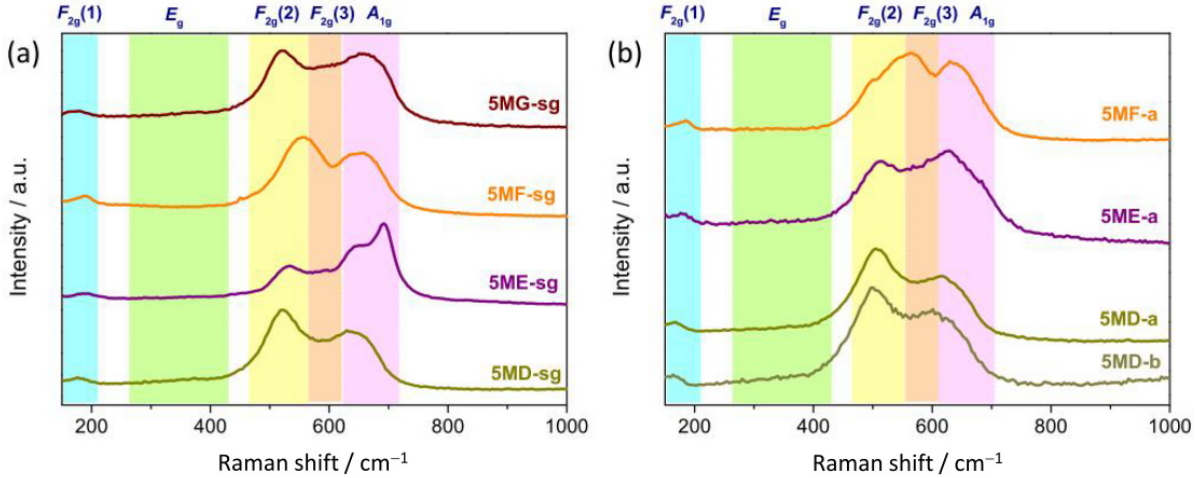

Figure 4. Averaged Raman spectra of pure single-phase HESOs produced via (**a**) sol-gel method and (**b**) electrospinning. The spectrum of sample 5MD-b is also reported.

In the $A^{2+}B^{3+}{}_2O_4$ spinel structure, cations occupy both octahedral and tetrahedral sites. Depending on the sites occupied by the A and B cations, normal, inverse or partial inverse spinel structures can be formed [65]. Frequencies and intensities of the Raman bands are sensitive to the type of cations, A^{2+} or B^{3+}, that occupy octahedral and tetrahedral sites. For example, the spectrum of chromate spinels (ACr_2O_4) changes with changing A cations [65]. All predicted Raman active modes are detected in the spectrum of $ZnCr_2O_4$, whereas the lowest wavenumber band $F_{2g}(1)$ is absent in that of $MgCr_2O_4$. By comparing the spectra of $FeCr_2O_4$ and $MgCr_2O_4$, noticeable changes in the relative intensity of bands are observed. Since in the chromate spinels, A^{2+} and Cr^{3+} cations are ordered in the tetrahedral and octahedral coordinated sites respectively, the observed variations in the Raman spectra can be attributed to the different divalent cations [65]. The same considerations hold if the trivalent cation changes. This may even cause the appearance of new vibration modes, as reported for $FeAl_2O_4$ and $FeCr_2O_4$ [65]. In addition, the presence of defects that generate distortions of the crystalline lattice contributes to shift the Raman bands and change their relative intensities [66].

However, in the case of HESOs, assessing the type of sites occupied by cations in the lattice is made even more difficult than in common spinels due to the inherent complexity of five-cation systems. In the present samples, the $F_{2g}(1)$ mode is detected between 160 and 220 cm^{-1}, whereas the very weak E_g mode is located between 250 and 420 cm^{-1}. Their relative intensities and frequency positions do not appreciably vary with the metal combinations (compare spectra shown in Figure 4). This finding points to the involvement of cations with oxidation state 3+ (namely Mn^{3+} and Fe^{3+}), present in the samples of all series (5MD/E/F/G). The higher frequency region of the spectra (>450 cm^{-1}), where the $F_{2g}(2)$, $F_{2g}(3)$ and A_{1g} modes are detected, seems to be more sensitive to the changes in metal combinations (compare the spectra of samples produced by the same method in Figure 4a). Conversely, samples produced by different methods or polymers, but having the same nominal composition, exhibit quite similar spectral profiles (compare the spectra of samples 5MD-sg, 5MD-a and 5MD-b). The case of the series 5ME represents the only exception and deserves further discussion. In the spectra of the electrospun samples, similar to each other, a weak shoulder is observed on the higher frequency side of the A_{1g} mode (at 625 cm^{-1}), as shown for sample 5ME-a (Figure 4a). The splitting of the A_{1g} mode into two branches is more sharply visible in the spectrum of sample 5ME-sg (Figure 4a), which closely resembles that of $(Co,Cr,Fe,Mn,Ni)_3O_4$ HESO synthesized via the solid-state reaction route [47]. This suggests that inversion may occur to some extent, owing to the replacement of some trivalent (divalent) cations by divalent (trivalent) cations in the octahedral (tetrahedral) sites [47,65].

3.3. Electrochemical Properties

The superior lithium-storage properties of rock-salt (Mg,Co,Ni,Cu,Zn) HEO, produced by solid-state reaction from an equimolar mixture of MgO, CoO, NiO, CuO and ZnO [11], as anode material have been pointed out by many groups [16,31]. For example, it was shown that such an HEO can deliver a reversible capacity of 920 mAh g^{-1} after 300 cycles at 100 mA g^{-1} and an excellent rate capability (600 mAh g^{-1} at 2 A g^{-1}) [16]. Furthermore, electrospun $(Mg_{0.2}Co_{0.2}Ni_{0.2}Cu_{0.2}Zn_{0.2})O$ NFs exhibit excellent cycling stability (390 mAh g^{-1} after 300 cycles at 500 mA g^{-1}) [36].

HEOs with spinel structures are particularly interesting because the unoccupied crystallographic sites should allow for the storing of additional Li ions, while the crystal structure should permit their fast diffusion. They have been the focus of in-depth studies [45,47,51]. $(Cr,Mn,Fe,Co,Ni)_3O_4$ was the first to be reported among them [47]. (Cr,Mn,Fe,Co,Ni) HESO prepared by solid-state reaction delivers specific capacities of 735, 586, 478, 361, 269 and 180 mAh g^{-1} at 0.05, 0.1, 0.2, 0.5, 1 and 2 A g^{-1}, respectively [45]. (Cr,Mn,Fe,Ni,Zn) HESO prepared by the same method retains a capacity of 387 mAh g^{-1} after 185 cycles at 0.5 A g^{-1} [70].

Here, two representative HESOs with the same nominal composition, $(Cr_{0.2}Mn_{0.2}Fe_{0.2}Co_{0.2}Zn_{0.2})_3O_4$, are considered: 5MF-sg, produced by SG route and; 5MF-b, prepared by ES using PAN as a polymer. Their electrochemical behavior as active anode materials in LIBs is preliminarily evaluated by carrying out measurements in the potential window of 0.01–3.0 V (versus Li/Li^+). Figure 5 displays the results obtained.

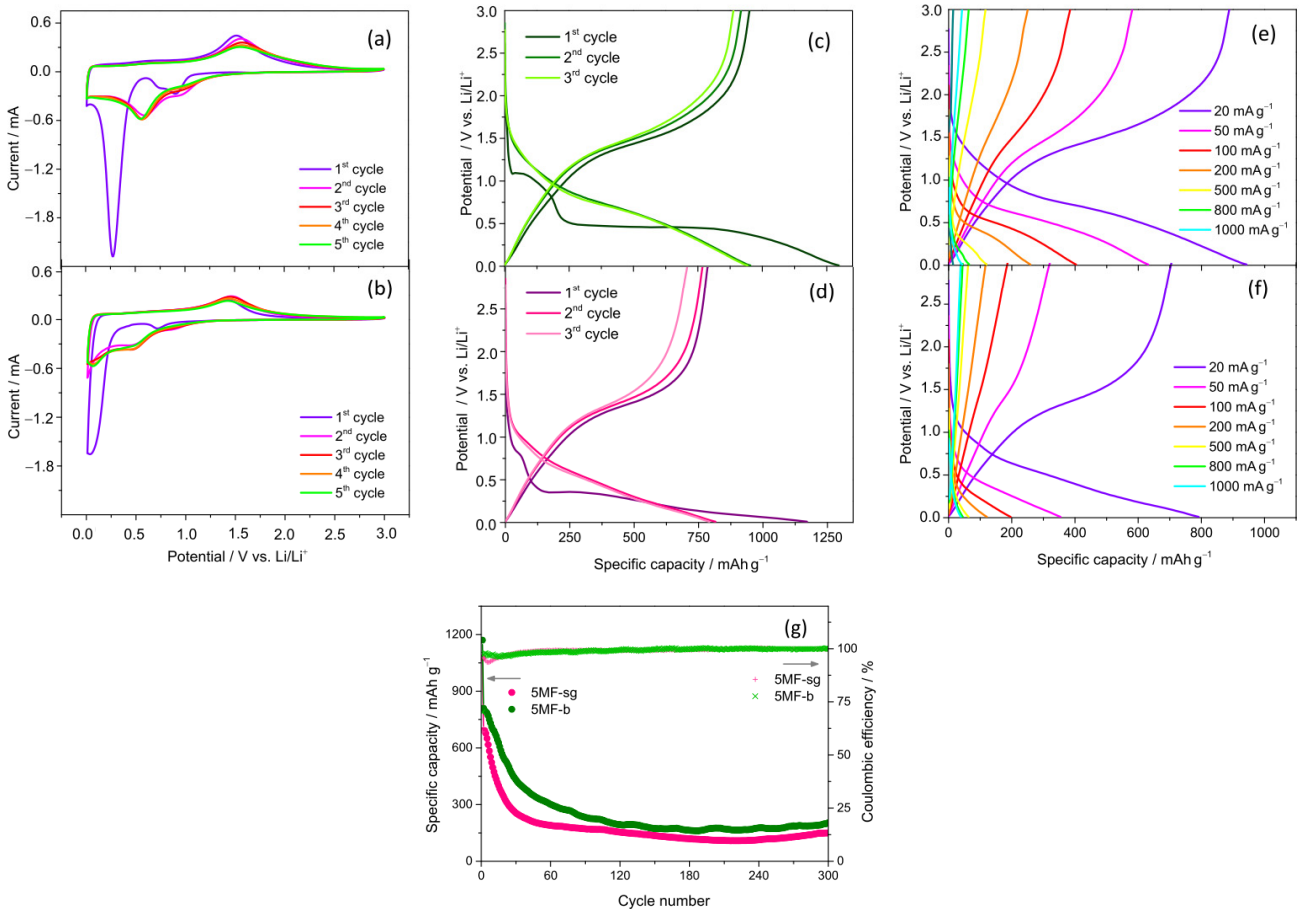

Figure 5. Electrochemical performance of HESOs (**a**,**c**,**e**) 5MF-b and (**b**,**d**,**f**) 5MF-sg in Li-ion half cells. (**a**,**b**) CV curves (scanning rate of 0.1 mV s^{-1}), (**c**,**d**) galvanostatic charge–discharge curves measured at 20 mA g^{-1} and (**e**,**f**) galvanostatic charge–discharge curves measured at different current density. (**g**) Cycling stability at a current density of 500 mA g^{-1}.

Figure 5a,b shows the cyclic voltammetry (CV) curves of the electrodes based on (Cr,Mn,Fe,Co,Zn) HESO NPs (5MF-sg) and (Cr,Mn,Fe,Co,Zn) HESO NFs (5MF-b) in the initial five cycles at a scan rate of 0.1 mV s^{-1}. These electrode materials display similar CV patterns, suggesting similar electrochemical processes of the two HESOs. The multiple anodic and cathodic peaks are associated with the Li^+ insertion–deinsertion process. In the first cycle, there is a strong cathodic peak located at around 0.4 V; this can be ascribed to the formation of solid electrolyte interphase (SEI) due to the decomposition of electrolyte [32]. The weaker cathodic peak at higher potential arises from the reduction of the HESO cations [71]. In the following anodic scan, the oxidation peaks may refer to the re-oxidation of metal elements into oxides. In the second cycle, the cathodic peak shifts to a higher potential and its intensity is significantly reduced, which might be caused by the irreversible reaction of the first lithiation process and pulverization of the electrode materials [16,72]. In the subsequent cycles, both the reduction and oxidation peaks are not overlapped very well, suggesting that the HESO anodes do not exhibit good stability and reversibility for the Li^+ insertion and extraction reactions.

To evaluate the capacity of the considered HESOs, galvanostatic charge–discharge tests were carried out at a current density of 20 mA g^{-1} (Figure 5c,d). In the first lithiation process, there is a clear potential plateau at around 0.45 V, corresponding to the reduction reaction of transition metals and the formation of the SEI layer, which is consistent with CV curves. The initial lithiation/delithiation capacities of anodes 5MF-b and 5MF-sg are 1297/950 and 1171/785 mAh g^{-1}, which correspond to initial Coulombic efficiencies (CE) of 73.2% and 60.5%, respectively. Higher capacities pertain to the HESO NFs. This is because electrospun fibrous structures provide direct current pathways along their axis, favoring the enhancement of capacity [36]. The initial capacity loss is associated with the SEI formation due to the decomposition of the electrolyte and structural rearrangement [48,72,73]. In the following cycles, all three samples show slopes rather than obvious plateaus during the discharge process, which could be associated with the different reaction voltage of multiple metals and structure rearrangement [45].

The rate capabilities of anodes 5MF-b and 5MF-sg were also evaluated, as shown in Figure 5e,f. With increasing current density, both samples show a fast capacity decay, implying a poor stability. The results of the long-term stability evaluation further prove that their structure is not stable (Figure 5g), possibly due to the pulverization of the HESO grains induced by the large volume changes occurring during the lithiation/delithiation process. The evaluation of the other pure single-phase samples (not shown for briefness) leads to similar results.

3.4. Strategies to Improve the Electrochemical Performance of the Investigated Samples

3.4.1. Incorporating Lithium in the HESO Lattice

Lökçu et al. [74] have recently evaluated the electrochemical performance of $(MgCoNiZn)_{1-x}Li_xO$, prepared by solid state reaction from milled MgO, CoO, NiO, ZnO, and Li_2O oxides, as anode material in LIBs. They have reported that the incorporation of lithium in the HEO lattice generates oxygen vacancies (OVs) and the higher the OV concentration in the anode, the higher its specific capacity. In particular, $(MgCoNiZn)_{0.65}Li_{0.35}O$ anode still delivers 610 mAh g^{-1} after 130 cycles at 1 A g^{-1} [74].

Here, a lithiated sample with nominal composition $Li_{1.8}(Cr_{0.2}Mn_{0.2}Fe_{0.2}Co_{0.2}Zn_{0.2})_3O_x$, coded as Li5MF-sg, is produced by the SG route by adding Li salt to the same solution utilized to prepare sample 5MF-sg. The incorporation of lithium in the HESO lattice leads to the formation of greater oxide particles (compare SEM, TEM and HRTEM images of samples 5MF-sg and Li5MF-sg in Figures S8 and S9), without affecting the spatial distribution of the elemental constituents (Figure S9e), the oxide phase (compare XRD patterns of the two samples in Figure S10a) and its spatial uniformity, as evaluated by MRS (Figure S11). Nevertheless, by comparing the micro-Raman spectra of the samples (Figure S10b), some differences come into view. In Li5MF-sg, a shoulder appears at 479 cm^{-1}, while the $F_{2g}(1)$ and A_{1g} modes downshift (the apparent peak positions move from 189 and 654 cm^{-1} to 181

and 634 cm^{-1}, respectively). Both these spectral changes are indicative of the generation of OVs induced by the incorporation of Li in the oxide lattice [75–77].

Figure 6 compares the electrochemical properties of anodes 5MF-sg and Li5MF-sg. Overall, CV and charge–discharge curves of $Li_{1.8}(Cr_{0.2}Mn_{0.2}Fe_{0.2}Co_{0.2}Zn_{0.2})_3O_x$ NPs (Figure 6b,d) do no not substantially differ from those of $(Cr_{0.2}Mn_{0.2}Fe_{0.2}Co_{0.2}Zn_{0.2})_3O_4$ NPs (Figure 6a,c), which is indicative of similar electrochemical processes. However, the strong reduction peak at the first cycle shifts to higher potential, and the peak intensity is stronger in the following cycles than that of 5MF-sg, which could be caused by Li incorporation in the HESO lattice. As reported in literature [46], the electrochemical process can be tailored by the incorporation of different elements in high-entropy oxide structures. The initial lithiation/delithiation capacities of anode Li5MF-sg (1112/733 mAh g^{-1}) are slightly lower than for anode 5MF-sg (1171/785 mAh g^{-1}), probably due to the larger particle size. Nonetheless, the corresponding initial CE is higher (66% against 60.5%); this value is comparable to that reported for $(FeCoNiCrMnZnLi)_3O_4$ prepared using the standard solid-state method (65%) [46].

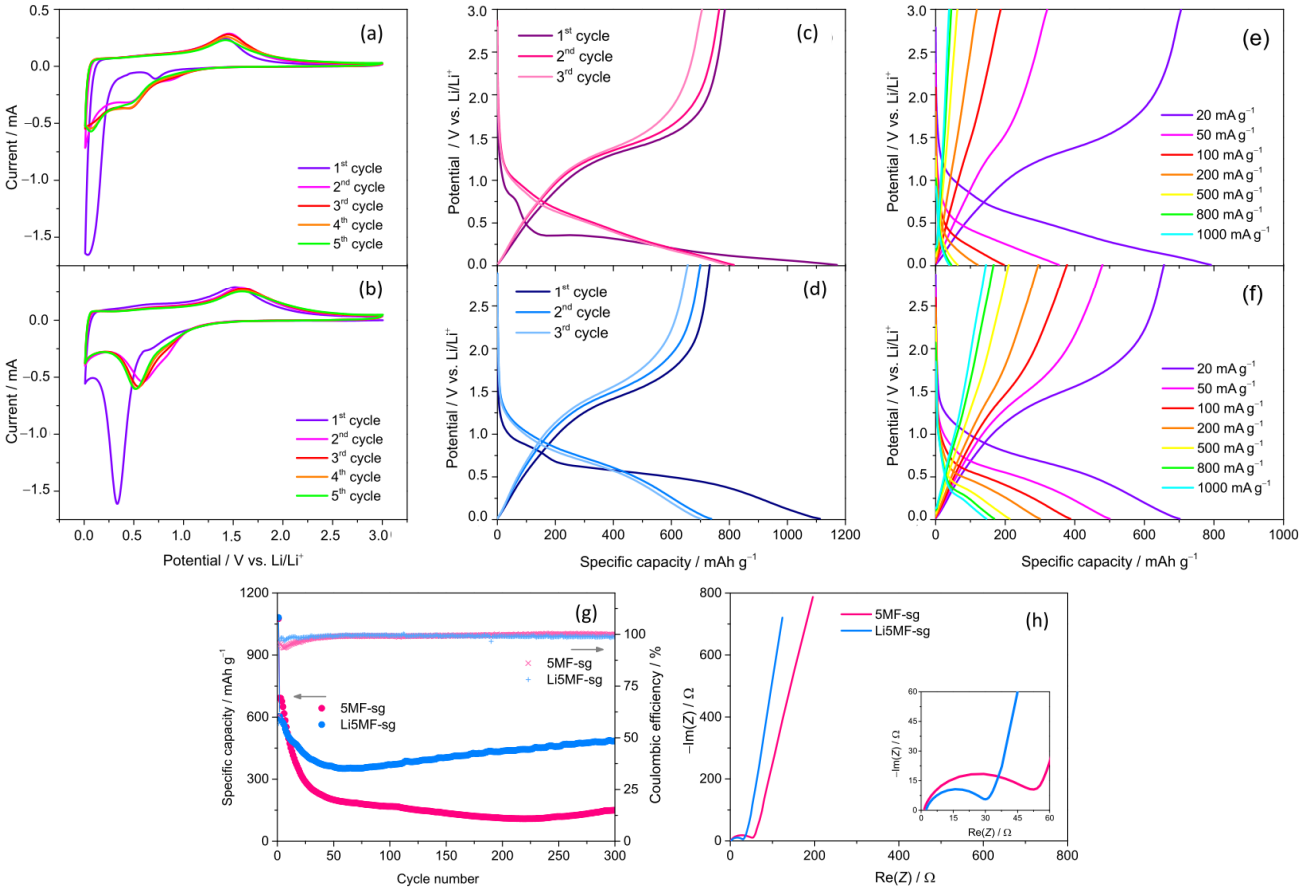

Figure 6. Electrochemical performance of samples (**a**,**c**,**e**) 5MF-sg, (**b**,**d**,**f**) Li5MF-sg in Li-ion half cells. (**a**,**b**) CV curves (scanning rate of 0.1 mV s^{-1}), (**c**,**d**) galvanostatic charge–discharge curves measured at 20 mA g^{-1} and (**e**,**f**) galvanostatic charge–discharge curves measured at different current density. (**g**) Cycling stability at a current density of 500 mA g^{-1} and (**h**) results of EIS measurements.

Figure 6e,f compares the results of the rate capability test carried out on anodes 5MF-sg and Li5MF-sg. With increasing current densities, the capacities gradually decrease because of the increased electrode polarization. Compared with 5MF-sg, Li5MF-sg achieves larger capacities and superior rate capability. When tested at 20, 50, 100, 200, 500 and 1000 mA g^{-1}, the Li5MF-sg electrode delivers good lithiation specific capacities of 702, 501, 388, 300, 213, 169 and 146 mAh g^{-1}, respectively. Additionally, when this sample is cycled at 500 mA g^{-1} for 300 cycles (Figure 6g), a reversible capacity as high as 484 mAh g^{-1} is

reached, which is much higher than that of 5MF-sg (150 mAh g^{-1}) and close to that reported for $(FeCoNiCrMnZnLi)_3O_4$ prepared using the standard solid-state method (522 mAh g^{-1}) after 100 cycles at the same rate [46]. The slightly increasing trend of specific capacity seems to be peculiar to materials with large particles [46].

The improved cycling stability could be ascribed to the increased configurational entropy deriving from the presence of the sixth metal in the combination and OVs generated, which induces the phase stabilization effect in the HESO [52,78]. The enhanced rate capability can be attributed to the improved ionic conductivity associated with the existence of a large number of OVs [46]. Figure 6h shows the results of EIS measurements performed to further evaluate Li^+ transfer behavior of the two anodes. Nyquist plots show a semicircle in the high-to-medium frequency region related to charge transfer resistance at the electrode/electrolyte interface; the straight line in the low-frequency region is associated with the Warburg impedance, which depends on the solid-state diffusion of Li^+-ions in the bulk electrode material. For anode Li5MF-sg, the semicircle diameter is much smaller than that of 5MF-sg, while the slope of the straight line is higher. These findings indicate greatly reduced charge transfer resistance and faster Li^+ transport in $Li_{1.8}(Cr_{0.2}Mn_{0.2}Fe_{0.2}Co_{0.2}Zn_{0.2})_3O_x$ NPs compared to $(Cr_{0.2}Mn_{0.2}Fe_{0.2}Co_{0.2}Zn_{0.2})_3O_4$ NPs. Both factors are responsible for the observed improvement in the electrochemical behavior.

3.4.2. Incorporating the Oxide in a Carbonaceous Matrix

Incorporating the active oxide particles in a carbonaceous matrix is a commonly adopted strategy to improve the electrochemical performance of anode materials prepared using different methods [43,44]. The carbon matrix favours the electrical transport and withstands the large volume changes, preventing the pulverization of the oxide particles.

Here, a composite carbon/HESO sample, coded as C5MF-b, is produced by ES followed by stabilization and carbonization. The sample, with nominal composition $C/(Cr_{0.2}Mn_{0.2}Fe_{0.2}Co_{0.2}Zn_{0.2})_3O_4$, exhibits a fibrous structure, similar to pure HESO (Figures S12 and S13). TEM/EDX analysis (Figure S14) reveals that the sample contains both C-poorer (Figure S13a,c) and C-richer NFs (Figure S14b,d). In the former, the oxide grains are generally larger (Figure S13a), whereas in the latter, they are finer (Figure S13b–d), in agreement with the well assessed ability of carbon to reduce the size of oxide grains and prevent their agglomeration [42–44]. In the micro-Raman spectrum of sample C5MF-b (Figure S15), the Raman fingerprints of both amorphous carbon [35,36] and (Cr,Mn,Fe,Co,Zn) HESO particles are detected.

Figure 7 compares the electrochemical properties of anodes 5MF-b and C5MF-b. Looking at their CV profiles (Figure 7a,b), it can be seen that the peak intensity and CV curve area of C5MF-b are higher than that of 5MF-b, implying that C/HESO NFs have better electrochemical kinetics [70]. Moreover, the second and third charge/discharge curves of anode C5MF-b are overlapped very well (Figure 7d), unlike those of 5MF-b (Figure 7c). This indicates that the composite NFs have better stability and reversibility for Li^+ insertion and extraction reactions than the pure HESO NFs [43]. Due to the specfic capacity of carbon (372 mAh g^{-1}) [42–44], the C/HESO NFs exhibit lower initial lithiation/delithiation capacities compared to HESO NFs (1159/777 against 1297/950 mAh g^{-1}). Figure 7e,f compares the results of the rate capability test carried out on anodes 5MF-b and C5MF-b. The measured delithiation capacities of C/HESO NFs are 834, 835, 784, 727, 610, 526, 471 and 345 mAh g^{-1} at 20, 50, 100, 200, 500, 1000 and 2000 mA g^{-1}, respectively. These values are higher than those measured in pure HESO NFs, especially at high current density, as expected [42–44]. In the long-term cyclability test (Figure 7g), the capacity decreases during the first 100 cycles and then increases. These capacity changes can be explained by the activation process and structural reconstruction associated with the

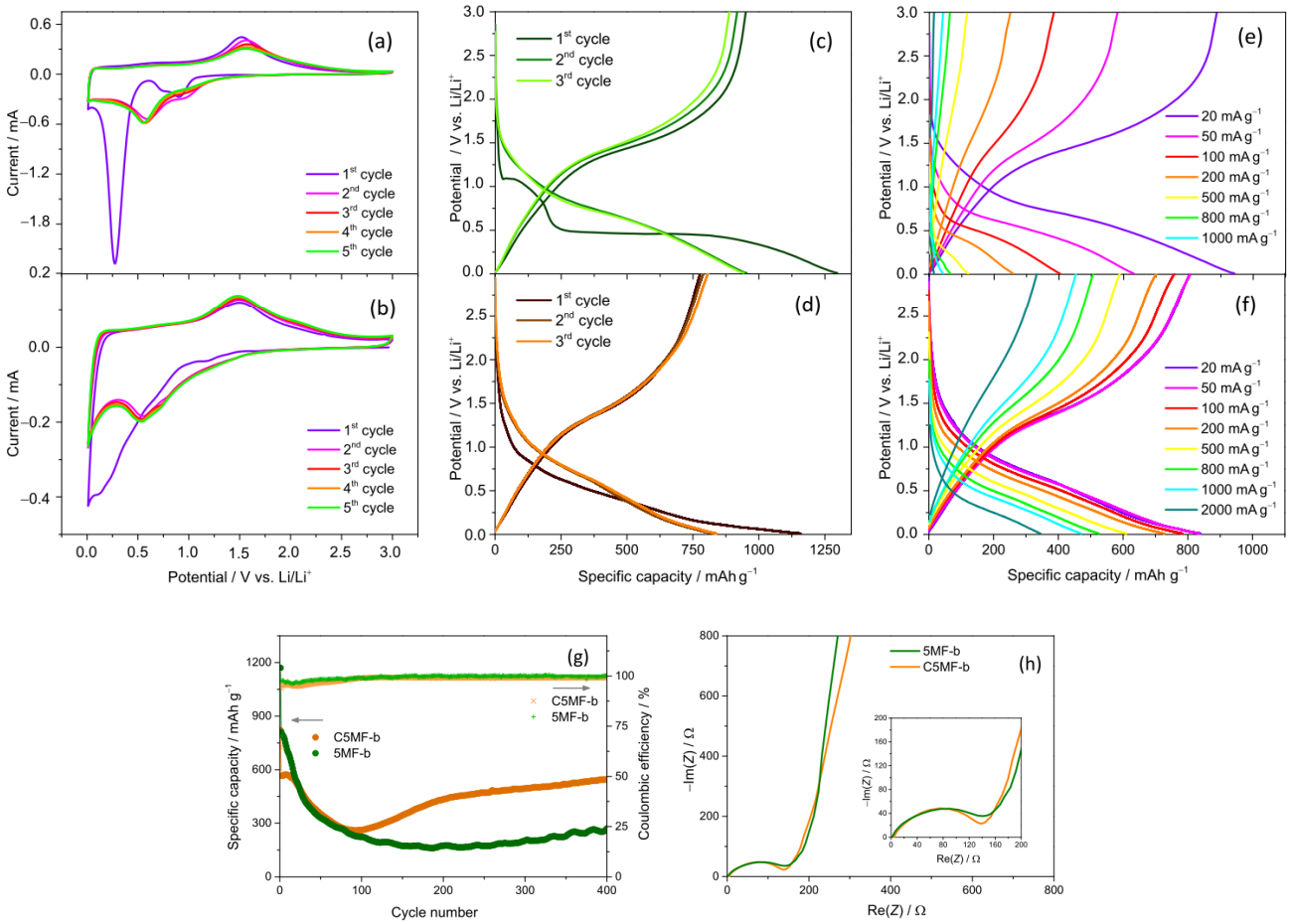

Figure 7. Electrochemical performance of samples (**a**,**c**,**e**) 5MF-b, (**b**,**d**,**f**) C5MF-b in the Li-ion half cells. (**a**,**b**) CV curves (scanning rate of 0.1 mV s^{-1}), (**c**,**d**) galvanostatic charge–discharge curves measured at 20 mA g^{-1} and (**e**,**f**) galvanostatic charge–discharge curves measured at different current density. (**g**) Cycling stability at a current density of 500 mA g^{-1} and (**h**) results of EIS measurements.

Active material [31]. After 400 cycles at a rate of 500 mA g^{-1}, C/HESO NFs deliver a capacity of around 545 mAh g^{-1}, which is much higher than that of 5MF-b (265 mAh g^{-1}). The results of EIS measurements (Figure 7h) evidence that the charge transfer resistance of C5MF-b is significantly lower than that of 5MF-b, confirming that the improvement in the electrochemical performance can be ascribed to the enhanced eletronic conductivity and mechanical stability promoted by carbon rather than to changes in the ionic transport.

4. Conclusions

This work demonstrates the possibility of producing pure single-phase HEOs with spinel structure (HESOs) under milder conditions than the standard solid-state techniques (i.e., with reduced environmental impact). Both XRD and Raman analyses highlight that the presence of copper or titanium in the equimolar combinations of the five metals considered favors the formation of secondary phase(s). SEM analysis shows that in ES syntheses, greater selectivity towards the NF formation is obtained using PAN as the polymer.

Pure single-phase HESOs are evaluated as active anode materials in lithium-ion batteries. They exhibit great potential (e.g., very high initial specific capacities) but poor rate capability and long-term stability. Hence, two possible strategies are proposed and successfully implemented to improve their electrochemical performance, as shown for two representative samples. The common strategy of incorporating carbon is demonstrated in the case of electrospun (Cr,Mn,Fe,Co,Zn) HESO, while the incorporation of lithium

in the HESO lattice is applied to the case of (Cr,Mn,Fe,Co,Zn) HESO produced via the sol-gel method.

The addition of Li enhances entropy and generates oxygen vacancies, thus improving stability and ionic transport. After 300 cycles at 0.5 A g^{-1}, $Li_{1.8}(Cr_{0.2}Mn_{0.2}Fe_{0.2}Co_{0.2}Zn_{0.2})_3O_x$ NPs deliver a much higher capacity than $(Cr_{0.2}Mn_{0.2}Fe_{0.2}Co_{0.2}Zn_{0.2})_3O_4$ NPs (484 against 150 mAh g^{-1}). The addition of C improves the electronic transport and mechanical stability. At 2 A g^{-1} rate, in composite $C/(Cr_{0.2}Mn_{0.2}Fe_{0.2}Co_{0.2}Zn_{0.2})_3O_4$ NFs, the measured delithiation capacity increases (from 15) to 345 mAh g^{-1}. Furthermore, after 400 cycles at a rate of 0.5 A g^{-1}, they still deliver 545 mAh g^{-1} against 265 mAh g^{-1} of pure $(Cr_{0.2}Mn_{0.2}Fe_{0.2}Co_{0.2}Zn_{0.2})_3O_4$ NFs.

Despite the presented results indicating the need to better tune the preparation conditions to improve the rate capability and cyclability, this preliminary study provides a further contribution to the understanding of HEOs. This is of great importance since these materials can potentially be utilized for the development of all components of rechargeable Li^+ and Na^+ ion batteries. Moreover, thanks to their generality, the approaches shown can be extensively applied to the optimization of HEO properties, even aimed at different applications.

Supplementary Materials: The following supporting information can be downloaded at: https://www.mdpi.com/article/10.3390/app12125965/s1, Figure S1: Schematic description of the experimental procedure followed to synthesize the HEO-samples; Figure S2: NF diameter distributions; Figure S3: Results of the SEM/EDX analysis on the most representative samples; Figure S4: TEM images; Figure S5: Results of the STEM/EDX analysis; Figure S6: Rietveld refinements; Table S1: results of Rietveld refinements; Figure S7: Micro-Raman spectra of representative samples; Figure S8: SEM and TEM images of samples 5MF-sg and Li5MF-sg; Figure S9: HRTEM images of samples 5MF-sg and Li5MF-sg; Figure S10: XRD and MRS images of samples 5MF-sg and Li5MF-sg; Figure S11: Micro-Raman spectra of samples 5MF-sg and Li5MF-sg; Figure S12: TEM images of sample C5MF-b. Inset: SAED pattern; Figure S13: HRTEM images of sample C5MF-b; Figure S14: Results of the STEM/EDX analysis on sample C5MF-b; Figure S15: Micro-Raman spectra of samples 5MF-b and C5MF-b.

Author Contributions: Conceptualization, S.S.; methodology, B.P., W.X., C.T. and F.P.; validation and formal analysis, W.X. and C.T.; data curation W.X., C.T. and S.S.; writing—original draft preparation W.X., C.T., M.G.M. and S.S.; writing—review and editing, S.P., N.P. and S.S.; funding acquisition, S.S., W.X. acknowledges the fellowship from the China Scholarship Council (CSC). All authors have read and agreed to the published version of the manuscript.

Funding: This research was partially funded by the Italian Ministry of University and Research (MUR), grant "PRIN 2017, 2017MCEEY4, Towards sustainable, high-performing, all-solid-state sodium-ion batteries".

Institutional Review Board Statement: Not applicable.

Informed Consent Statement: Not applicable.

Data Availability Statement: The raw data and processing aids, required to reproduce the findings of this work, cannot be shared at this time as they form the basis for an ongoing study.

Acknowledgments: Christoph Erdmann is acknowledged for electron microscopy measurements. B.P. and S.S. gratefully thank the Italian Ministry of University and Research (MUR) for the financial support of this study through a grant "PRIN 2017, 2017MCEEY4, Towards sustainable, high-performing, all-solid-state sodium-ion batteries".

Conflicts of Interest: The authors declare no conflict of interest.

References

1. Miracle, D.B.; Senkov, O.N. A critical review of high entropy alloys and related concepts. *Acta Mater.* **2017**, *122*, 448–511. [CrossRef]
2. Yeh, J.W.; Lin, S.J. Breakthrough applications of high-entropy materials. *J. Mater. Res.* **2018**, *33*, 3129–3137. [CrossRef]
3. Musicó, B.L.; Gilbert, D.; Ward, T.Z.; Page, K.; George, E.; Yan, J.; Mandrus, D.; Keppens, V. The emergent field of high entropy oxides: Design, prospects, challenges, and opportunities for tailoring material properties. *APL Mater.* **2020**, *8*, 040912. [CrossRef]
4. Oses, C.; Toher, C.; Curtarolo, S. High-entropy ceramics. *Nat. Rev. Mater.* **2020**, *5*, 295–309. [CrossRef]
5. Braic, V.; Vladescu, A.; Balaceanu, M.; Luculescu, C.R.; Braic, M. Nanostructured multi-element (TiZrNbHfTa)N and (TiZrNbHfTa)C hard coatings. *Surf. Coat. Technol.* **2012**, *211*, 117–121. [CrossRef]
6. Jin, T.; Sang, X.; Unocic, R.R.; Kinch, R.T.; Liu, X.; Hu, J.; Liu, H.; Dai, S. Mechanochemical-assisted synthesis of high-entropy metal nitride via a soft urea strategy. *Adv. Mater.* **2018**, *30*, 1707512. [CrossRef]
7. Castle, E.; Csanádi, T.; Grasso, S.; Dusza, J.; Reecet, M. Processing and properties of high-entropy ultra-high temperature carbides. *Sci. Rep.* **2018**, *8*, 8609. [CrossRef]
8. Zhou, J.; Zhang, J.; Zhang, F.; Niu, B.; Lei, L.; Wang, W. High-entropy carbide: A novel class of multicomponent ceramics. *Ceram. Int.* **2018**, *44*, 22014–22018. [CrossRef]
9. Gild, J.; Zhang, Y.; Harrington, T.; Jiang, S.; Hu, T.; Quinn, M.C.; Mellor, W.M.; Zhou, N.; Vecchio, K.; Luo, J. High-entropy metal diborides: A new class of high-entropy materials and a new type of ultrahigh temperature ceramics. *Sci. Rep.* **2016**, *6*, 37946. [CrossRef]
10. Zhang, R.Z.; Gucci, F.; Zhu, H.; Chen, K.; Reece, M.J. Data-driven design of ecofriendly thermoelectric high-entropy sulfides. *Inorg. Chem.* **2018**, *57*, 13027–13033. [CrossRef]
11. Rost, C.M.; Sachet, E.; Borman, T.; Moballegh, A.; Dickey, E.C.; Hou, D.; Jones, J.L.; Curtarolo, S.; Maria, J.-P. Entropy-stabilized oxides. *Nat. Commun.* **2015**, *6*, 8485. [CrossRef]
12. Sarkar, A.; Wang, Q.; Schiele, A.; Chellali, M.R.; Bhattacharya, S.S.; Wang, D.; Brezesinski, T.; Hahn, H.; Velasco, L.; Breitung, B. High-entropy oxides: Fundamental aspects and electrochemical properties. *Adv. Mater.* **2019**, *31*, 1806236. [CrossRef]
13. Dabrowa, J.; Stygar, M.; Mikuła, A.; Knapik, A.; Mroczka, K.; Tejchman, W.; Danielewski, M.; Martin, M. Synthesis and microstructure of the (Co, Cr, Fe, Mn, Ni)$_3$O$_4$ high entropy oxide characterized by spinel structure. *Mater. Lett.* **2018**, *216*, 32–36. [CrossRef]
14. Mao, A.; Quan, F.; Xiang, H.; Zhang, Z.; Kuramoto, K.; Xia, A. Facile synthesis and ferrimagnetic property of spinel (CoCrFeMnNi)$_3$O$_4$ high-entropy oxide nanocrystalline powder. *J. Mol. Struct.* **2019**, *1194*, 11–18. [CrossRef]
15. Biesuz, M.; Spiridigliozzi, L.; Dell'Agli, G.; Bortolotti, M.; Sglavo, V.M. Synthesis and sintering of (Mg, Co, Ni, Cu, Zn)O entropy-stabilized oxides obtained by wet chemical methods. *J. Mater. Sci.* **2018**, *53*, 8074–8085. [CrossRef]
16. Qiu, N.; Chen, H.; Yang, Z.; Sun, S.; Wang, Y.; Cui, Y. A high entropy oxide ($Mg_{0.2}Co_{0.2}Ni_{0.2}Cu_{0.2}Zn_{0.2}O$) with superior lithium storage performance. *J. Alloy. Compd.* **2019**, *777*, 767–774. [CrossRef]
17. Sarkar, A.; Breitung, B.; Hahn, H. High entropy oxides: The role of entropy, enthalpy and synergy. *Scr. Mater.* **2020**, *187*, 43–48. [CrossRef]
18. Grzesik, Z.; Smoła, G.; Miszczak, M.; Stygar, M.; Dabrowa, J.; Zajusz, M.; Swierczek, K.; Danielewski, M. Defect structure and transport properties of (Co, Cr, Fe, Mn, Ni)$_3$O$_4$ spinel-structured high entropy oxide. *J. Eur. Ceram. Soc.* **2020**, *40*, 835–839. [CrossRef]
19. Chen, K.; Pei, X.; Tang, L.; Cheng, H.; Li, Z.; Li, C.; Zhang, X.; An, L. A five-component entropy-stabilized fluorite oxide. *J. Eur. Ceram. Soc.* **2018**, *38*, 4161–4164. [CrossRef]
20. Anandkumar, M.; Bhattacharya, S.; Deshpande, A.S. Low temperature synthesis and characterization of single phase multi-component fluorite oxide nanoparticle sols. *RSC Adv.* **2019**, *9*, 26825–26830. [CrossRef]
21. Zhao, C.; Ding, F.; Lu, Y.; Chen, L.; Hu, Y.-S. High-entropy layered oxide cathodes for sodium-ion batteries. *Angew. Chem. Int. Ed.* **2020**, *59*, 264–269. [CrossRef]
22. Teng, Z.; Zhu, L.; Tan, Y.; Zeng, S.; Xia, Y.; Wang, Y.; Zhang, H. Synthesis and structures of high-entropy pyrochlore oxides. *J. Eur. Ceram. Soc.* **2020**, *40*, 1639–1643. [CrossRef]
23. Jiang, S.; Hu, T.; Gild, J.; Zhou, N.; Nie, J.; Qin, M.; Harrington, T.; Vecchio, K.; Luo, J. A new class of high-entropy perovskite oxides. *Scr. Mater.* **2018**, *142*, 116–120. [CrossRef]
24. Sarkar, A.; Djenadic, R.; Wang, D.; Hein, C.; Kautenburger, R.; Clemens, O.; Hahn, H. Rare earth and transition metal based entropy stabilised perovskite type oxides. *J. Eur. Ceram. Soc.* **2018**, *38*, 2318–2327. [CrossRef]
25. Okejiri, F.; Zhang, Z.; Liu, J.; Liu, M.; Yang, S.; Dai, S. Room-temperature synthesis of high-entropy perovskite oxide nanoparticle catalysts through ultrasonication-based method. *ChemSusChem* **2020**, *13*, 111–115. [CrossRef]
26. Bérardan, D.; Franger, S.; Dragoe, D.; Meena, A.K.; Dragoe, N. Colossal dielectric constant in high entropy oxides. *Phys. Status Solidi RRL* **2016**, *10*, 328–333. [CrossRef]
27. Sarkar, A.; Loho, C.; Velasco, L.; Thomas, T.; Bhattacharya, S.S.; Hahn, H.; Djenadic, R. Multicomponent equiatomic rare earth oxides with a narrow band gap and associated praseodymium multivalency. *Dalton Trans.* **2017**, *46*, 12167–12176. [CrossRef]
28. Bérardan, D.; Franger, S.; Meena, A.K.; Dragoe, N. Room temperature lithium superionic conductivity in high entropy oxides. *J. Mater. Chem. A* **2016**, *4*, 9536–9541. [CrossRef]

29. Chen, H.; Fu, J.; Zhang, P.; Peng, H.; Abney, C.W.; Jie, K.; Liu, X.; Chi, M.; Dai, S. Entropy-stabilized metal oxide solid solutions as CO oxidation catalysts with high-temperature stability. *J. Mater. Chem. A* **2018**, *6*, 11129–11133. [CrossRef]
30. Gao, Y.; Liu, Y.; Yu, H.; Zou, D. High-entropy oxides for catalysis: Status and perspectives. *Appl. Catal. A Gen.* **2022**, *631*, 118478. [CrossRef]
31. Sarkar, A.; Velasco, L.; Wang, D.; Wang, Q.; Talasila, G.; de Biasi, L.; Kübel, C.; Brezesinski, T.; Bhattacharya, S.S.; Hahn, H.; et al. High entropy oxides for reversible energy storage. *Nat. Commun.* **2018**, *9*, 3400. [CrossRef]
32. Chen, T.-Y.; Wang, S.-Y.; Kuo, C.-H.; Huang, S.-C.; Lin, M.-H.; Li, C.-H.; Chen, H.-Y.T.; Wang, C.-C.; Liao, Y.-F.; Lin, C.-C.; et al. In operando synchrotron X-ray studies of a novel spinel $(Ni_{0.2}Co_{0.2}Mn_{0.2}Fe_{0.2}Ti_{0.2})_3O_4$ high-entropy oxide for energy storage applications. *J. Mater. Chem. A* **2020**, *8*, 21756–21770. [CrossRef]
33. Wang, S.-Y.; Chen, T.-Y.; Kuo, C.-H.; Lin, C.-C.; Huang, S.-C.; Lin, M.-H.; Wang, C.-C.; Chen, H.-Y. Operando synchrotron transmission X-ray microscopy study on (Mg, Co, Ni, Cu, Zn)O high-entropy oxide anodes for lithium-ion batteries. *Mater. Chem. Phys.* **2021**, *274*, 125105. [CrossRef]
34. Guo, H.-X.; Wang, W.-M.; He, C.-Y.; Liu, B.-H.; Yu, D.-M.; Liu, G.; Gao, X.-H. Entropy-assisted high-entropy oxide with a spinel structure toward high-temperature infrared radiation materials. *ACS Appl. Mater. Interfaces* **2022**, *14*, 1950–1960. [CrossRef]
35. Zhang, J.; Yan, J.; Calder, S.; Zheng, Q.; McGuire, M.A.; Abernathy, D.L.; Ren, Y.; Lapidus, S.H.; Page, K.; Zheng, H.; et al. Long-range antiferromagnetic order in a rocksalt high entropy oxide. *Chem. Mater.* **2019**, *31*, 3705–3711. [CrossRef]
36. Triolo, C.; Xu, W.; Petrovičovà, B.; Pinna, N.; Santangelo, S. Evaluation of entropy-stabilised $(Mg_{0.2}Co_{0.2}Ni_{0.2}Cu_{0.2}Zn_{0.2})O$ oxides produced via solvothermal method or electrospinning as anodes in lithium ion batteries. *Adv. Funct. Mater.* **2022**, 2202892. [CrossRef]
37. Liu, J.; Ma, C.; Wang, L.; Ren, K.; Ran, H.; Feng, D.; Du, H.; Wang, Y. Single-phase formation mechanism and dielectric properties of sol-gel-derived $Ba(Ti_{0.2}Zr_{0.2}Sn_{0.2}Hf_{0.2}Ce_{0.2})O_3$ high-entropy ceramics. *J. Mater. Sci. Technol.* **2022**, *130*, 103–111. [CrossRef]
38. Li, Z.; Zhou, F.; Xu, B.; Guo, D. Characterization of novel high-entropy $(La_{0.2}Nd_{0.2}Sm_{0.2}Dy_{0.2}Yb_{0.2})_2Zr_2O_7$ electrospun ceramic nanofibers. *Ceram. Int.* **2022**, *48*, 12074–12078. [CrossRef]
39. Xing, Y.; Dan, W.; Fan, Y.; Li, X. Low temperature synthesis of high-entropy $(Y_{0.2}Yb_{0.2}Sm_{0.2}Eu_{0.2}Er_{0.2})_2O_3$ nanofibers by a novel electrospinning method. *J. Mater. Sci. Technol.* **2022**, *103*, 215–220. [CrossRef]
40. Wang, G.; Qin, J.; Feng, Y.; Feng, B.; Yang, S.; Wang, Z.; Zhao, Y.; Wei, J. Sol–gel synthesis of spherical mesoporous high-entropy oxides. *ACS Appl. Mater. Interfaces* **2020**, *12*, 45155–45164. [CrossRef]
41. Santangelo, S. Electrospun nanomaterials for energy applications: Recent advances. *Appl. Sci.* **2019**, *9*, 1049. [CrossRef]
42. Pantò, F.; Fan, Y.; Frontera, P.; Stelitano, S.; Fazio, E.; Patanè, S.; Marelli, M.; Antonucci, P.; Neri, F.; Pinna, N.; et al. Are electrospun carbon/metal oxide composite fibers relevant electrode materials for Li-Ion batteries? *J. Electrochem. Soc.* **2016**, *163*, A2930. [CrossRef]
43. Pantò, F.; Fan, Y.; Stelitano, S.; Fazio, E.; Patanè, S.; Frontera, P.; Antonucci, P.; Pinna, N.; Santangelo, S. Are electrospun fibrous membranes relevant electrode materials for li-ion batteries? The case of the $C/Ge/GeO_2$ composite fibers. *Adv. Funct. Mater.* **2018**, *28*, 1800938. [CrossRef]
44. Han, X.; Russo, P.A.; Goubard-Bretesché, N.; Patanè, S.; Santangelo, S.; Zhang, R.; Pinna, N. Exploiting the condensation reactions of acetophenone to engineer carbon-encapsulated Nb_2O_5 nanocrystals for high-performance Li and Na energy storage systems. *Adv. Energy Mater.* **2019**, *9*, 1902813. [CrossRef]
45. Wang, D.; Jiang, S.; Duan, C.; Mao, J.; Dong, Y.; Dong, K.; Wang, Z.; Luo, S.; Liu, Y.; Qi, X. Spinel-structured high entropy oxide $(FeCoNiCrMn)_3O_4$ as anode towards superior lithium storage performance. *J. Alloy. Compd.* **2020**, *844*, 156158. [CrossRef]
46. Duan, C.; Tian, K.; Li, X.; Wang, D.; Sun, H.; Zheng, R.; Wang, Z.; Liu, Y. New spinel high-entropy oxides $(FeCoNiCrMnXLi)_3O_4$ (X = Cu, Mg, Zn) as the anode material for lithium-ion batteries. *Ceram. Int.* **2021**, *47*, 32025–32032. [CrossRef]
47. Sun, Z.; Zhao, Y.; Sun, C.; Ni, Q.; Wang, C.; Jin, H. High entropy spinel-structure oxide for electrochemical application. *Chem. Eng. J.* **2022**, *431*, 133448. [CrossRef]
48. Chen, H.; Qiu, N.; Wu, B.; Yang, Z.; Sun, S.; Wang, Y. A new spinel high-entropy oxide $(Mg_{0.2}Ti_{0.2}Zn_{0.2}Cu_{0.2}Fe_{0.2})_3O_4$ with fast reaction kinetics and excellent stability as an anode material for lithium ion batteries. *RSC Adv.* **2020**, *10*, 9736–9744. [CrossRef]
49. Stygar, M.; Dąbrowa, J.; Moździerz, M.; Zajusz, M.; Skubida, W.; Mroczka, K.; Berent, K.; Swierczek, K.; Danielewski, M. Formation and properties of high entropy oxides in Co-Cr-Fe-Mg-Mn-Ni-O system: Novel $(Cr, Fe, Mg, Mn, Ni)_3O_4$ and $(Co, Cr Fe,Mg, Mn)_3O_4$ high entropy spinels. *J. Eur. Ceram. Soc.* **2020**, *40*, 1644–1650. [CrossRef]
50. Liang, B.; Ai, Y.; Wang, Y.; Liu, C.; Ouyang, S.; Liu, M. Spinel-type $(FeCoCrMnZn)_3O_4$ high-entropy oxide: Facile preparation and supercapacitor performance. *Materials* **2020**, *13*, 5798. [CrossRef]
51. Nguyen, T.X.; Patra, J.; Chang, J.K.; Ting, J.M. High entropy spinel oxide nanoparticles for superior lithiation–delithiation performance. *J. Mater. Chem. A* **2020**, *8*, 18963–18973. [CrossRef]
52. Mao, A.; Xiang, H.Z.; Zhang, Z.G.; Kuramoto, K.; Zhang, H.; Jia, Y. A new class of spinel high-entropy oxides with controllable magnetic properties. *J. Magn. Magn. Mater.* **2020**, *497*, 165884. [CrossRef]
53. Raul, P.K.; Senapati, S.; Sahoo, A.K.; Umlong, I.M.; Devi, R.R.; Thakur, A.J.; Veer, V. CuO nanorods: A potential and efficient adsorbent in water purification. *RSC Adv.* **2014**, *4*, 40580–40587. [CrossRef]
54. Alhumaimess, M.S.; Essawy, A.A.; Kamel, M.M.; Alsohaimi, I.H.; Hassan, H.M.A. Biogenic-mediated synthesis of mesoporous Cu_2O/CuO nano-architectures of superior catalytic reductive towards nitroaromatics. *Nanomaterials* **2020**, *10*, 781. [CrossRef] [PubMed]

55. Wang, J.L.; Mukherjee, S.; Nisbet, D.R.; Birbilis, N.; Chen, X.B. In vitro evaluation of biodegradable magnesium alloys containing micro-alloying additions of strontium, with and without zinc. *J. Mater Chem. B* **2015**, *3*, 8874–8883. [CrossRef]
56. Hu, G.; Zhong, M.; Guo, C. Microstructures and high temperature tensile properties of As-Aged Mg-6Zn-1Mn-4Sn-(01, 0.5 and 1.0) Y alloys. *Metals* **2019**, *9*, 1. [CrossRef]
57. Thota, S.; Prasad, B.; Kumar, J. Formation and magnetic behaviour of manganese oxide nanoparticles. *J. Mater. Sci. Eng. B* **2010**, *167*, 153–160. [CrossRef]
58. Sharrouf, M.; Awad, R.; Roumié, M.; Marhaba, S. Structural, Optical and room temperature magnetic study of Mn_2O_3 nanoparticles. *Mater. Sci. Appl.* **2015**, *6*, 850–859.
59. Qiao, H.; Wei, Z.; Yang, H.; Zhu, L.; Yan, X. Preparation and characterization of NiO nanoparticles by anodic arc plasma Method. *J. Nanomater.* **2009**, *2009*, 1–5. [CrossRef]
60. Hong, S.J.; Mun, H.J.; Kim, B.J.; Kim, Y.S. Characterization of nickel oxide nanoparticles synthesized under low temperature. *Micromachines* **2021**, *12*, 1168. [CrossRef]
61. Deori, K.; Deka, S. Morphology oriented surfactant dependent CoO and reaction time dependent Co_3O_4 nanocrystals from single synthesis method and their optical and magnetic properties. *CrystEngComm* **2013**, *15*, 8465. [CrossRef]
62. Lutz, H.D.; Müller, B.; Steiner, H.J. Lattice vibration spectra. LIX. Single crystal infrared and Raman studies of spinel type oxides. *J. Solid State Chem.* **1991**, *90*, 54–60. [CrossRef]
63. Kumar, P.R.; Jung, Y.H.; Bharathi, K.K.; Lim, C.H.; Kim, D.K. High capacity and low cost spinel Fe_3O_4 for the Na-ion battery negative electrode materials. *Electrochim. Acta* **2014**, *146*, 503–510. [CrossRef]
64. Abdellatif, M.H.; Azab, A.A.; Salerno, M. Effect of rare earth doping on the vibrational spectra of spinel Mn-Cr ferrite. *Mater. Res. Bull.* **2018**, *97*, 260–264. [CrossRef]
65. D'Ippolito, V.; Andreozzi, G.B.; Bersani, D.; Lottici, P.P. Raman fingerprint of chromate, aluminate and ferrite spinels. *J. Raman Spectrosc.* **2015**, *46*, 1255–1264. [CrossRef]
66. Rivas-Murias, B.; Salgueirino, V. Thermodynamic CoO–Co_3O_4 crossover using Raman spectroscopy in magnetic octahedron-shaped nanocrystals. *J. Raman Spectrosc.* **2017**, *48*, 837–841. [CrossRef]
67. Lazarević, Z.; Jovalekić, Č.; Milutinović, A.; Sekulić, D.; Ivanovski, V.N.; Rečnik, A.; Cekic, B.; Romčević, N.Ž. Nanodimensional spinel $NiFe_2O_4$ and $ZnFe_2O_4$ ferrites prepared by soft mechanochemical synthesis. *J. Applied Physics* **2013**, *113*, 187221. [CrossRef]
68. Supriya, S.; Kumar, S.; Kar, M. Structural and electrical properties of CFO nanoparticle-filled PVA. *J. Electron. Mater.* **2019**, *48*, 3612–3623. [CrossRef]
69. Laguna-Bercero, M.A.; Sanjuán, M.L.; Merino, R.I. Raman spectroscopic study of cation disorder in poly-and single crystals of the nickel aluminate spinel. *J. Phys. Condens. Matter* **2007**, *19*, 186217. [CrossRef]
70. Xiao, B.; Wu, G.; Wang, T.; Wei, Z.; Sui, Y.; Shen, B.; Qi, J.; Wei, F.; Meng, Q.; Ren, Y.; et al. High entropy oxides $(FeNiCrMnX)_3O_4$ (X = Zn, Mg) as anode materials for lithium ion batteries. *Ceram. Int.* **2021**, *47*, 33972–33977. [CrossRef]
71. Cao, Z.; Yang, Y.; Qin, J.; He, J.; Su, Z. Co_3O_4 polyhedron@MnO_2 nanotube composite as anode for high-performance lithium-ion batteries. *Small* **2021**, *17*, 2008165. [CrossRef] [PubMed]
72. Ghigna, P.; Airoldi, L.; Fracchia, M.; Callegari, D.; Anselmi-Tamburini, U.; D'angelo, P.; Pianta, N.; Ruffo, R.; Cibin, G.; Oliveira de Souza, D.; et al. Lithiation mechanism in high-entropy oxides as anode materials for Li-ion batteries: An operando XAS study. *ACS Appl. Mater. Interfaces* **2020**, *12*, 50344–50354. [CrossRef] [PubMed]
73. Wang, Q.; Sarkar, A.; Wang, D.; Velasco, L.; Azmi, R.; Bhattacharya, S.S.; Bergfeldt, T.; Duvel, A.; Heitjans, P.; Brezesinski, T.; et al. Multi-anionic and -cationic compounds: New high entropy materials for advanced Li-ion batteries. *Energy Environ. Sci.* **2019**, *12*, 2433. [CrossRef]
74. Lokcu, E.; Toparli, C.; Anik, M. Electrochemical performance of $(MgCoNiZn)_{1-x}Li_xO$ high-entropy oxides in lithium-ion batteries. *ACS Appl. Mater. Interfaces* **2020**, *12*, 23860–23866. [CrossRef] [PubMed]
75. Fukushima, H.; Kozu, T.; Shima, H.; Funakubo, H.; Uchida, H.; Katoda, T.; Nishida, K. Evaluation of oxygen vacancy in ZnO using Raman spectroscopy. In Proceedings of the 2015 Joint IEEE International Symposium on the Applications of Ferroelectric (ISAF), International Symposium on Integrated Functionalities (ISIF), and Piezoelectric Force Microscopy Workshop (PFM), Singapore, 24–27 May 2015. [CrossRef]
76. Chapron, D.; Cordero, F.; Fontana, M.D. Characterization on of oxygen vacancies in $SrTiO_3$ by means of inelastic and Raman speectroscopy. *J. Appl. Phys.* **2019**, *126*, 154101. [CrossRef]
77. De Castro Silva, I.; Sigoli, F.A.; Mazali, I.O. Reversible oxygen vacancy generation on pure CeO_2 nanorods evaluated by in situ Raman spectroscopy. *J. Phys. Chem. C* **2017**, *121*, 12928–12935. [CrossRef]
78. Wang, B.; Yao, J.; Wang, J.; Chang, A. Spinel-type high-entropy $(Co_{0.2}Mn_{0.2}Fe_{0.2}Zn_{0.2}Ti_{0.2})_3O_4$ oxides constructed from disordered cations and oxygen vacancies. *J. Alloy. Compd.* **2022**, *897*, 163188. [CrossRef]